Journal of Applied Fluid Mechanics, Vol. 17, No. 6, pp. 1306-1321, 2024.
Available online at www.jafmonline.net, ISSN 1735-3572, EISSN 1735-3645.
https://doi.org/10.47176/jafm.17.6.2309

Effects of the Reynolds Number on the Efficiency and Stall Mechanisms in a Three-stage Axial Compressor

E. Zhou†, P. Lei, C. Fan, W. Zhang, K. Liu and S. Cheng

High Speed Aerodynamics Institute, China Aerodynamics Research and Development Center, Mianyang 621000, China

†*Corresponding Author Email:* zhouenmin@cardc.cn

ABSTRACT

The Reynolds number (*R*e) is an important parameter that can affect compressor performance. This study experimentally and numerically investigated the effect of *R*e variations on the efficiency and stall mechanisms for a three-stage axial flow compressor. In the experiment, the total pressure ratio, polytropic efficiency, and stalling mass flow rate were measured in a *R*e range varying from 1,100,000 to 55,000 to elucidate the *R*e effects. Unsteady three-dimensional numerical simulations were implemented to understand the stall mechanisms. The results indicate that the compressor efficiency and stall–pressure ratio begin to decrease remarkably as *R*e is reduced below a critical value, which is 220,000 in the case of the compressor studied. At a low *R*e, losses caused by the secondary flow near the hub and shroud increase remarkably, and the extended boundary layer separations at the blade suction surface further decrease the efficiency. The variation in *R*e changes the stall-initiated location. At higher Reynolds numbers, the interaction between the corner separation at the hub of stator 1 and the leakage flow through the blade tip gap induces a large vortex, which seriously blocks the blade passage. The blocking effect spreads to the aft stage and extends to higher spans, which results in the stall of the whole compressor. However, the blocking effect at the hub disappears at *R*e =55,000, and the interaction of the blade boundary layer separation near the shroud of rotor 1 and the tip leakage vortex causes a large blockage and then induces stall. The *R*e variation changes the radial flow transportation because of the varying effect on the aerodynamic performance of each blade element at different spans. This significantly influences the extent of the vortex near the end wall and ultimately changes the stall mechanisms.

Article History

Received September 12, 2023
Revised January 21, 2024
Accepted February 1, 2024
Available online March 27, 2024

Keywords:

Compressor performance
Numerical and experimental research
Reynolds number variation
Critical Reynolds number
Stall separation
Blocking flow
Secondary flow

1. INTRODUCTION

Axial flow compressors should have high efficiency and sufficient stall margins to ensure the economical and safe operation of aero engines under any operating condition (Hathaway, 2007). In particular, the stall-limiting line in a compressor map cannot be exceeded during operation to avoid potential engine failure. The Reynolds number (*Re*) is an important parameter that considerably affects compressor performance. A *Re* based on the real chord and inlet velocity can decrease by one order of magnitude for military aircrafts when operating at high altitudes. In addition, the operating *Re* also changes when scaling a state-of-the-art compressor to different sizes in the design process to save valuable design resources and time. A decrease in *Re* may lead to high flow losses and change the stall-limiting line as *Re* decreases below a critical value. Therefore, understanding the mechanisms through which the *Re* affects compressor efficiency and stall mechanisms is critical.

Most related studies have focused on the effects of the *Re* on compressor efficiency. Weinberg & Wyzykowski (2000) tested the PW545 jet engine, which was originally designed to operate at a 13.7 km altitude. They reported that the overall engine efficiency decreased dramatically above 18.3 km because of the low air density at the high altitude. Therefore, the loss mechanism due to a low *Re* should be fully understood to improve engine performance.

A low *Re* can cause laminar boundary layer separation with no reattachment downstream, which results in a large recirculating flow with consequent

NOMENCLATURE

b	chord length of rotor 1 at the middle span	T_0	total temperature at the inlet
c_p	$(p-p_0)/(\rho v^2/2)_0$	T_s	blade passing period
L	axial length of the compressor	v	absolute velocity
m	mass flow rate	v_z	axial component of velocity
n_0	fitting coefficient in Eq. (1)	w	relative velocity
n_1	fitting coefficient in Eq. (1)	Δ	relative change of any parameter
n_2	fitting coefficient in Eq. (2)	π	total pressure ratio
n_3	fitting coefficient in Eq. (4)	ρ	density
p	static pressure	η	polytropic efficiency
P	total pressure	η_m	efficiency on the meridional plane
P_0	total pressure at the inlet	μ	viscosity at inlet
Re	Reynolds number, $\rho wb/\mu$	σ	recovery coefficient of total pressure
T	total temperature	γ	polytropic coefficient
Subscripts			
0	inlet of blade passage	*Ns*	near-stall condition
*	stagnation parameter	*ref*	reference condition, Re =1,100,000
i	arbitrary position on the meridional plane		

increased aerodynamic loss. Much effort has been made to determine the loss mechanisms of airfoil or blade cascades (Citavy & Norbury, 1977; Enomoto et al., 2000; Schreiber et al., 2002; Hobson et al., 2001; Hayashibara et al., 2006; Lazaro et al., 2017; Myose & Hayashibara, 2009; Back et al., 2010; Carullo et al., 2011; Bolinches-Gisbert et al., 2020; Wang et al., 2021). Citavy and Norbury (1977) observed a substantial effect of *Re* on the growth and bursting of a separation bubble and the consequent effects on the aerodynamic performance of the cascade. Wang et al. (2020) claimed that the laminar separation bubble mainly determined the loss generation process of a compressor airfoil. Lázaro et al. (2017) studied the profile loss in an intermediate pressure compressor aerofoil under design and off-design flow incidences. They found that the profile loss depended on the *Re* at close to nominal incidence, but the profile loss rapidly increased as the incidence increased and became independent of the *Re*. Bolinches-Gisbert et al. (2020) reported that the trend of losses with varying *Re* had two regimes, where the losses scaled with Re^{-1} or $Re^{-1/2}$. Kok et al. (2015) proposed a semiempirical method that could be used as an alternative method for determining the entropy generation rate in a low *Re* compressor cascade. Kato et al. (2011) described the important effect of the relative motion of a casing wall on the tip leakage flow and cascade performance at a low *Re*.

Except for the loss in the blade profile, the loss in the end wall region is significant at a low *Re*. Pantelidis & Hall (2017) experimentally studied aerodynamic losses due to 3D effects in the end wall regions of a compact compressor operating at a low *Re.* They found high tip loss, a hub separation that grew at a low *Re* in the rotor, and high hub loss in the stator. Diehl et al. (2020) compared the *Re* effect and increased relative tip clearance resulting from manufacturing limitations on the efficiency of a small-scale compressor. They claimed that the *Re* dependent loss was clearance independent over the whole compressor operating range, and increasing the clearance had a much greater effect on the compressor performance. Ni et al. (2019) reported that the *Re* mainly affected the passage wake near the shroud and tip clearance flow in the impeller, which caused a loss associated with the boundary layer in the hub of the vaned diffuser in the centrifugal compressor stage. Kim et al. (2018) showed that compressor performance decreased slowly with decreasing *Re* but decreased significantly below the threshold of 200,000 because of the large separation in diffuser vanes. Below a critical *Re*, Zheng et al. (2013) reported that the interaction between the tip leakage flow and the separated boundary layer caused severe loss in a transonic compressor. Therefore, the exponent was commonly used in determining the relationship between efficiency degradation and Reynolds number (Wassell, 1968; Zhang, 2020). However, the proposed empirical correlation methods were usually proven to work well under design conditions, but they provided inaccurate calculations under off-design conditions.

Ever-improving understanding of the loss mechanisms due to *Re* effects has led to vast explorations of control methods for improving compressor efficiency at a low *Re*. Pym et al. (2019) explored the potential of integrated leading-edge tubercles to improve blade performance at *Re* values between 15,000 and 60,000. Their experimental results showed that the implementation of tubercles did not lead to a performance enhancement but could generate streamwise vortices at ultralow Reynolds numbers. Valdes et al. (2018) studied the influence of *Re* on compressor efficiency by changing working fluids and reported that the efficiency as a function of *Re* improved with increasing fluid density. Maffioli et al. (2015) explored the available design space for compact axial compressor blade sections by investigating the effect of thickness distributions and the pitch-to-chord ratio at a *Re* =50,000. High-turning compressor airfoils (Sonoda et al., 2003; Schreiber et al., 2004), Gurney flaps (Myose et al., 2006), solidity (Hayashibara, et al., 2013), leading edge roughness (Im et al., 2013), and surface roughness (Back et al., 2012; Wang et al., 2021) have also been investigated to reduce losses induced by a low *Re*.

The effect of *Re* on compressor stability is another important issue. Hadavandi et al. (2018) investigated the stalling behaviour, inception, and stall-cell flow field for two different Reynolds numbers. Hutchings & Hall (2020) experimentally investigated the effects of *Re* on the flow characteristics of a compact compressor both pre-stall and in-stall. They found that the blockage associated with hub corner separation and tip clearance caused stall, and the frequency of the stall cell decreased by 2.8% as the Re was reduced from 60,000 to 20,000. Chen et al. (2020) reported that surge flow was likely to increase or decrease when the compressor size was increased or decreased, respectively, for a turbocharger compressor; however, these authors did not explain the underlying reasons. Zhao et al. (2015) claimed that the complex flow near the blade tip was the key factor for the limited flow stability under a high *Re* and low *Re*, and the decrease in Re enhanced the surface boundary layer separation and radial transport of low-energy fluid. Chen et al. (2019) observed the phenomenon of rotating instability, which was controlled by the interaction of the tip leakage flow and incoming flow at a high *Re*, whereas at a low *Re*, the tip leakage flow became weak, and the radial flow from the hub to the tip induced by the suction surface flow separation was dominant in the tip region.

The above studies have confirmed the significant impact of *Re* on compressor efficiency and stability. However, the mechanism by which *Re* affects compressor efficiency, especially in multistage compressors, is not fully understood. A method for predicting the compressor efficiency caused by *Re* variations under off-design conditions also needs to be discussed. With respect to compressor stability, spikes and modal waves (McDougall et al., 1990; Camp & Day, 1998) are considered two typical types of stall inception. Changes in working conditions, including rotating speed (Wilke et al., 2005), tip clearance size (Matthias et al., 2017), and inflow conditions (Arshad et al., 2018; Sun et al., 2018), can alter compressor stall characteristics. However, whether a decrease in *Re* can change stall characteristics has not been determined. Therefore, there is a strong motivation to study the mechanisms of the effect of *Re* on compressor efficiency and possible changes in stall mechanisms in a multistage environment.

In the present study, a three-stage axial flow compressor was explored experimentally and numerically under five Reynolds numbers ranging from 1,100,000 to 55,000. The influence of *Re* on compressor efficiency under design and off-design conditions was analysed, and empirical correlation methods were utilized to predict the *Re* effects. Then, a quantitative analysis of the near-stall flow fields was conducted to understand the stall mechanisms at different Reynolds numbers. Finally, the change in compressor stall mechanisms caused by *Re* variations was discussed.

2. TEST FACILITY AND INSTRUMENTATION

The experiment was conducted on a three-stage axial

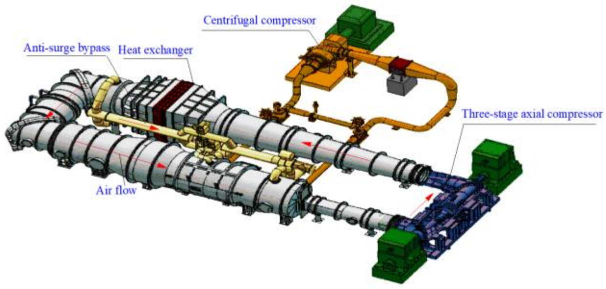

Fig. 1 Closed-return wind tunnel sketch

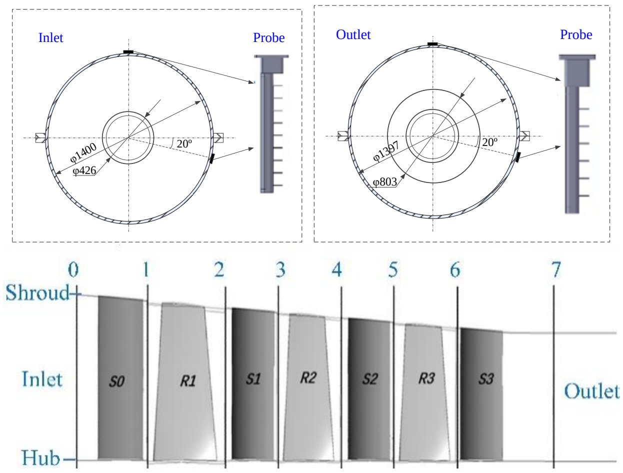

Fig. 2 Meridional view of the compressor and instrumentation installation

flow compressor. The compressor was powered by variable-speed induction motors, and it produced airflow in a wind tunnel, which was a closed-return, variable-density tunnel with a fixed-geometry, ventilated test section (Fig. 1). In the experiment, this compressor was utilized to study the effect of *Re* on compressor performance.

The axial compressor consisted of an inlet guide vane (IGV), rotor 1, stator 1, rotor 2, stator 2, rotor 3, and stator 3 with 52, 25, 44, 31, 48, 31, and 48 blades, respectively. Figure 2 shows a meridional view of the compressor. The maximum speed was 3600 rpm, and the compressor was tested at 2593 rpm in the experiment. The running tip clearance size of the rotors was 1.8 mm, and the tip clearance size between the stator tip and the hub was 1.5 mm. The IGV, stator 1, stator 2, and stator 3 had variable geometries, and the nominal setting angles were bound to be 11°, 24°, 26° and 26° for the test speed, respectively. The other compressor parameters are shown in Table 1.

In the experiment, the whole device was evacuated by using two vacuum pumps to realize continuous adjustment of the air density to adjust the inlet pressure of the axial compressor. Five kinds of inlet total pressure, 100, 50, 20, 10 and 5 kPa, which generated Reynolds numbers of 1,100,000, 550,000, 220,000, 110,000, and 55,000, were studied. The total temperature was kept at 288 K for different Reynolds numbers using a heat exchanger (Fig. 1). The total pressure ratio, efficiency, and mass flow rate of the compressor were measured under different inlet conditions. Total pressure and

Table 1 Compressor parameters at the test speed

Parameter	value
Mass flow (kg/s)	76
Total pressure ratio	1.25
Adiabatic efficiency	0.88
Rotational speed (rpm)	2593
Inlet tip relative Mach number	0.6
Hub/tip ratio of R1	0.64
Tip gap of rotor and stator (mm)	1.8
Inlet diameter (m)	1.4

temperature were measured using radial rakes (consisting of several probes). The radial rakes were installed approximately 2.1L (L is the distance from section 0 to section 7; Fig. 2) upstream of the first rotor to reduce the influence of the rakes on the inflow condition, and 2.3L downstream of the last stator to ensure that the outflow fully mixed. Two radial rakes, which were separated by 110° in the circumferential direction, were installed at each test section. Nine probes, including five total pressure probes and four total temperature probes, were used for the rake at the inlet, and six probes, including three total pressure probes and three total temperature probes, were utilized for the rake at the outlet. The mass flow rate through the compressor was measured using a calibrated orifice plate. Before data collection, the compressor was kept in stable operation for at least 30 min after the operating conditions were changed. The data measured in 10 s with a sampling frequency of 10 Hz were averaged for each operating point. The measuring accuracies were 0.2%, 0.5%, and 0.5% for the total pressure, temperature, and mass flow rate, respectively. References (Zhou et al., 2015; Zhang et al., 2017) provided more information about the tested facility and measurement method.

3. NUMERICAL MODEL

The commercial CFD software ANSYS CFX was used to study the effect of *Re* on compressor performance. A computational mesh with a hexahedral structure was generated using a turbogrid. The computational domain of the compressor is shown in Fig. 3. Multiple passages were modelled for all the blades with the periodical assumption that the flow was identical at the periodic boundary to reduce computational time. The blade numbers were not changed, and the passage numbers (shown in Fig. 3) of different blade rows were adjusted to make the circumferential coverage angle of each blade as close as possible. The numbers of blade passage used in each blade row are shown in Table 2. The inlet passage was extended upstream by approximately two times the chord length of S0, and the outlet passage was extended downstream by approximately two times the chord length of S3. The tip clearance of the rotors and the hub clearance of the stators were meshed with 25 points along the radial direction. The mesh was stretched towards all the solid boundaries to meet the resolution requirement of $y^{+}\leq 2$. The grid numbers of each single-blade passage are shown in Table 2. The mesh used for the multiple passages contained approximately 12,980,000 grid elements.

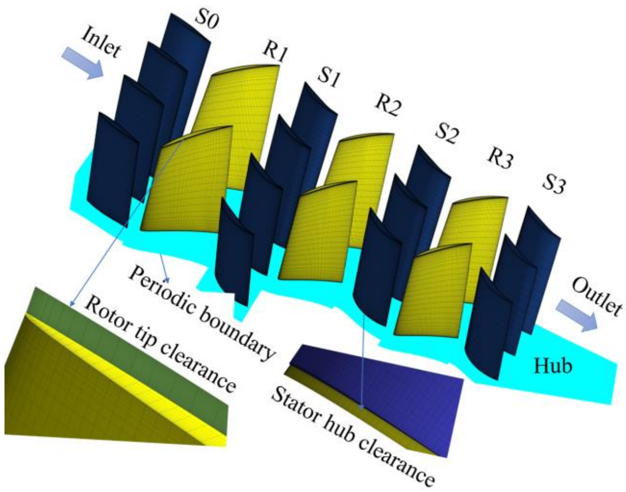

Fig. 3 Grid topology of the three-stage compressor

Table 2 Mesh information of the compressor

Part	Blade numbers	Passage numbers	Element numbers of each blade row
S0	52	4	2396256
R1	25	2	1708706
S1	44	4	2340680
R2	31	2	1801440
S2	48	3	1697076
R3	31	2	1233468
S3	48	3	1803960

The CFX platform was utilized to solve the fully three-dimensional steady RANS equations. The k-Omega model (Toyotaka et al., 2003; Farahani et al., 2012) was used to model turbulence. A second-order resolution scheme was employed to discretize the advection term. The total pressure and total temperature were varied according to the experiment at the inlet boundary to change the inflow Reynolds numbers. The mass flow rates at the outlet boundary were varied to obtain different operating points. Adiabatic and nonslip conditions were imposed on all the solid walls. Steady-state simulations were utilized to obtain a compressor performance map, and unsteady simulations were performed at key points to determine the flow mechanisms. The “mixed plane method” and “transient rotor stator” were used to model the interfaces between the rotating rotors and stationary stators in steady and unsteady simulations, respectively. The steady simulation results were set as the initial values of the unsteady simulations. The time step in unsteady simulations was set to 1/7779 s, corresponding to the time interval for rotor 1 to travel 2°. The convergence criterion was satisfied when the parameters, including the residuals, efficiency, and mass flow rate at the inlet, did not change during steady simulations, and the periodic fluctuations of the parameters were treated as the convergence criterion during unsteady simulations.

Grid independence studies were implemented using the multiple passages model. The change of compressor efficiency under the design point with grid element numbers is shown in Table 3. The mesh used herein was proven to produce grid-independent results when the

Table 3 Grid independence verification

Element numbers	η
0.48×10^7	89.00%
0.78×10^7	89.30%
1.12×10^7	89.52%
1.30×10^7	89.56%
1.58×10^7	89.57%

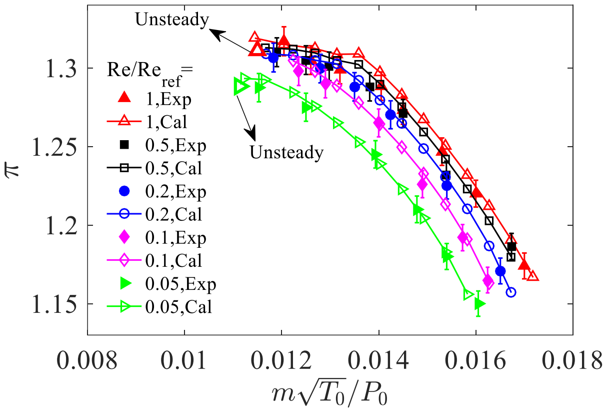

(a) Total pressure ratio

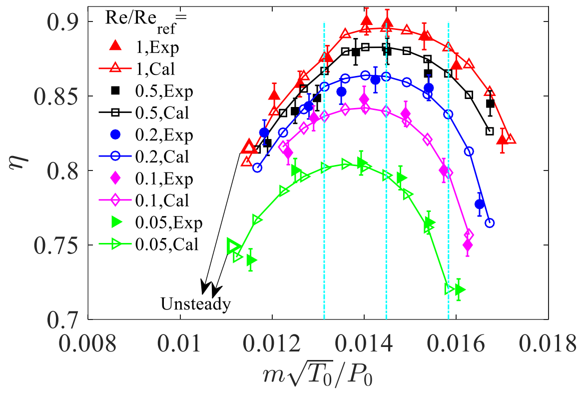

(b) Polytropic efficiency

Fig. 4 Compressor characteristics under different Reynolds numbers

element numbers are above 11,213,000. Figure 4 shows the compressor characteristics obtained via the experiment and steady calculation results under the different Reynolds numbers. The time-averaged values of the unsteady results under near stall conditions for Re/Re_{ref}=0.05 and Re/Re_{ref}=1 are also shown. The mass flow rate in the abscissa was corrected using the respective inlet total pressure and total temperature of each Reynolds number. The reference Re_{ref} was set to 1,100,000. The choked mass flow rate was accurately calculated using the numerical model under different Reynolds numbers. The predicted pressure ratio was slightly higher than the experimental value, but most calculated values were within the error zone. The calculated stall-pressure ratio agreed well with the experimental data, and the decreasing trend of the stall-pressure ratio with decreasing *Re* was also well captured. The compressor efficiency was well predicted, and the deviation in compressor efficiency between the experiment and the calculation rose slightly under near stall conditions. Therefore, the numerical model

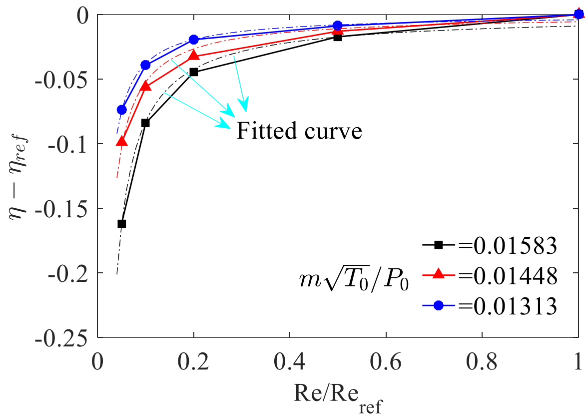

(a) Fitting of the compressor losses

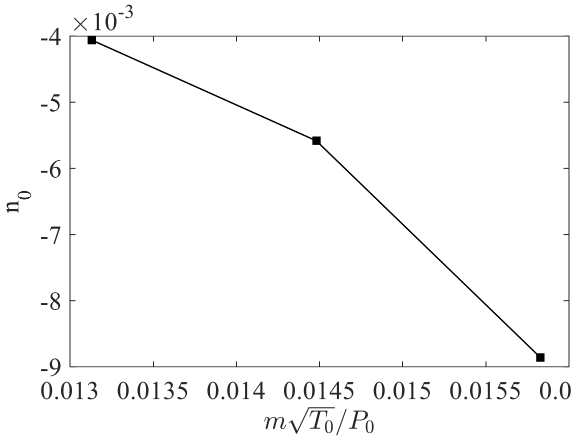

(b) Fitting coefficient n_0

Fig. 5 Changes in compressor losses with *Re* under different operating conditions

accurately captured the influence of *Re* on the performance of the three-stage compressor.

4. RESULTS AND DISCUSSION

4.1 Effect on Compressor Efficiency

The inlet velocity triangle of R1 and the inlet Mach number are kept constant at the same corrected mass flow rate (marked with dashed lines, as shown in Fig. 4) under different Reynolds numbers. The compressor efficiency is markedly reduced due to the decrease in *Re*, and the degradation degree varies under different operating conditions. Figure 5 shows the increase in the compressor loss evaluated by η-η_{ref} due to the decrease in *Re*. The reference η_{ref} is set as the efficiency at the Re_{ref}. Wassell (1968) surveyed data of twenty axial compressors and proposed an empirical approach for predicting the effect of *Re* on compressor efficiency under the design condition. The close relationship between the compressor efficiency and *Re* was verified with the assumption that $1-\eta=n_0\left(Re\right)^{-n_1}$. The parameter n_1 is determined by the shock loss, which is related to the Mach number and the relevant geometrical parameters. For the present compressor, the value of n_1 is fixed because the compressor operates under subsonic conditions (no shockwave loss), and the geometric parameters are kept constant. The parameter n_1 is calculated as 0.97 for the compressor to minimize the fitting standard deviation under different operating mass flow rates. The parameter n_0 which is shown in Fig. 5 (b), should vary with the operating conditions to predict the efficiency changes precisely. The correction equation is then defined as

$$\eta-\eta_{ref}=n_0\left(Re\right)^{-n_1},n_1=0.97 \tag{1}$$

The relationship between n_0 and the corrected mass flow rate is nonlinear, as shown in Fig. 5 (b). Therefore, the changes in compressor efficiency with Re under off-design conditions are difficult to predict using the parameters under the design conditions.

Based on test data of several multi-stage compressors, Schaffler (1980) proposed another empirical approach to predict the decreasing efficiency with decreasing Re and obtained good agreement with Wassell (1968) correlation. The method uses normalized changes in compressor efficiency and Re, which are defined as

$$\frac{1-\eta}{1-\eta_{ref}}=\left(\frac{Re}{Re_{ref}}\right)^{n_2} \tag{2}$$

The fitting results and the independent variable n_2 are illustrated in Fig. 6. The fitting accuracy is not as good as that in Eq. (1), but the relationship between n_2 and the corrected mass flow rates is nearly linear. Therefore, the changes in compressor efficiency under off-design conditions can be predicted using the parameters under the design conditions by changing only n_2.

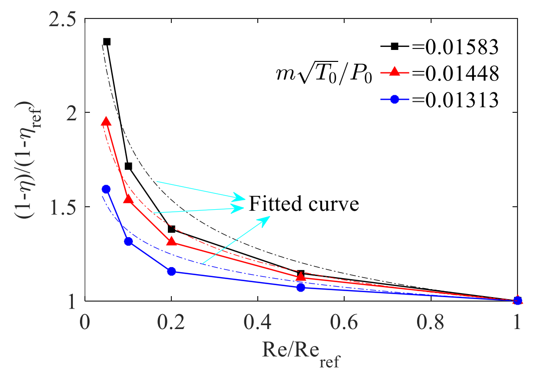

(a) Fitting of the normalized efficiency changes

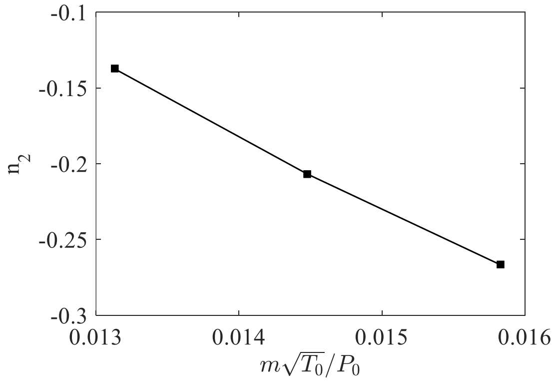

(b) Fitting coefficient n_2

Fig. 6 Normalized changes in compressor efficiency with *Re* under different operating conditions

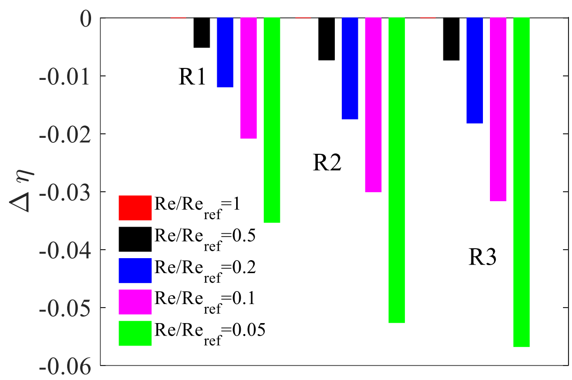

(a) Rotor blades

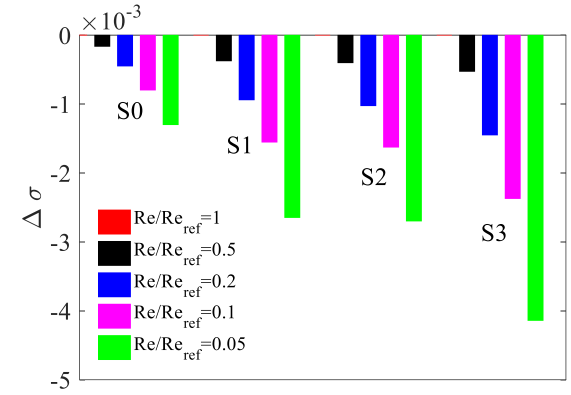

(b) Stator blades

Fig. 7 Relative changes in compressor efficiency for each blade under the design condition at different Reynolds numbers

Figure 7 shows the relative changes of efficiency for each blade under different inlet Reynolds numbers compared with the reference to understand the reasons for the decline in compressor efficiency. The compressor operates under the design condition ($m\sqrt{T_0}/P_0=0.01448$) for different Reynolds numbers. The rotor polytropic efficiency (η) is defined using the total pressure and total temperature at the inlet and outlet of each blade, and the stator efficiency is defined as the recovery coefficient (σ) of the total pressure. With decreasing Re, the penalty on the efficiency of each blade increases. Moreover, the influence on the efficiency of all the blades increases from the inlet to the outlet. This phenomenon implies that the factors that decrease the compressor efficiency are amplified step by step following the flow direction.

To determine the location that causes increased losses, the efficiency η_m on the meridional plane is defined as

$$\eta_m=\frac{\left(P_i/P_0\right)^{\frac{\gamma-1}{\gamma}}-1}{\left(T_i/T_0\right)-1} \tag{3}$$

The total pressure and total temperature used are azimuthally averaged values. The efficiency η_m represents the average flow loss for the air approaching downstream. The relative changes in efficiency

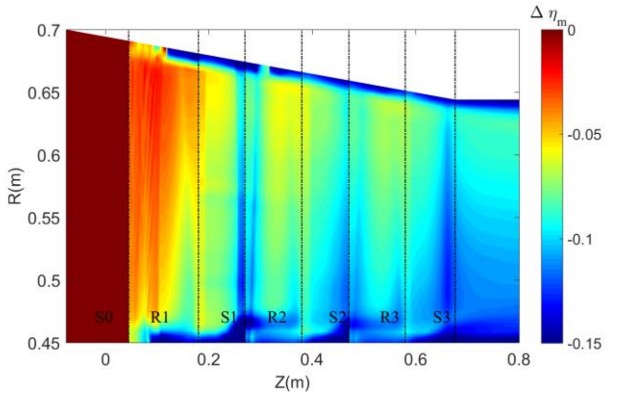

Fig. 8 Relative changes in efficiency on the meridional plane between *Re*/*Re*ref =0.05 and *Re*/*Re*ref =1 under the design condition

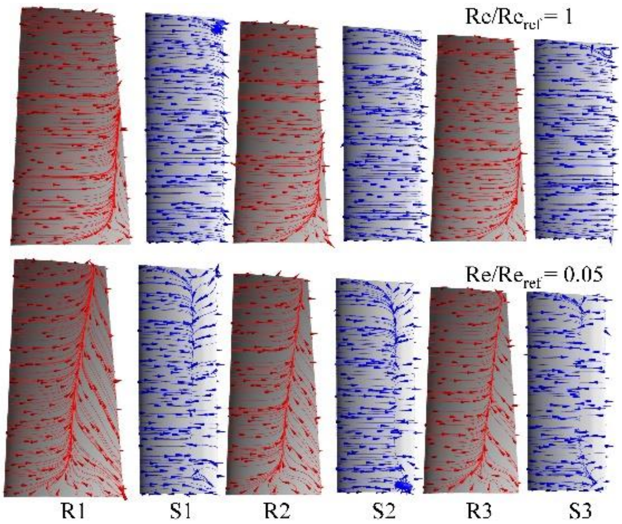

Fig. 9 Distributions of limiting streamlines on the blade suction surface under the design condition

($\Delta\eta_m = \eta_m - \eta_{m,ref}$) between Re/Re_{ref}=0.05 and Re/Re_{ref}=1 are calculated for the design condition ($m\sqrt{T_0}/P_0 = 0.01448$) and are shown in Fig. 8. The negative values represent the absolute magnitude of efficiency degradation resulting from the decrease in *Re*. The compressor efficiency is reduced along the whole span, especially in the tip and hub regions. A high loss near the end wall was also observed by Hutchings & Hall (2020). In the tip region, the domain of large efficiency degradation is limited near the shroud, but the loss at the hub extends towards the upper spans, which results in the trend of efficiency degradation shown in Fig. 7.

Figure 9 shows the limiting streamlines on the suction surface of all the blades, and Fig. 10 depicts the normalized total pressure at the outlet of S3. The deficit in total pressure represents the flow loss. At a high *Re*, slight corner separation is observed at the hub of all the rotor blades. However, the corner separation is remarkably aggravated by the decrease in *Re*, and the separation lines stretch up to the blade tip. A decrease in *Re* also causes flow separation at the suction surface of all stator blades. As a result, the domain of high loss near the hub and the loss magnitude increase. Moreover, the blade wake thickness and total pressure loss increase

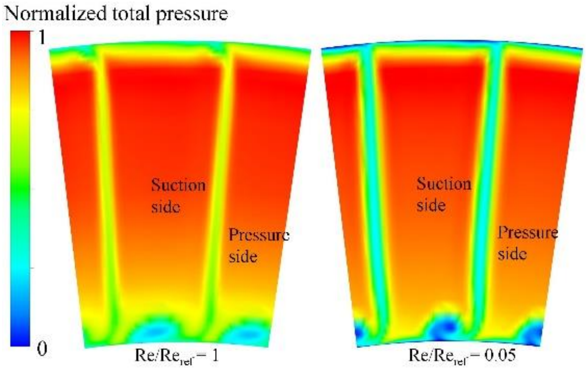

Fig. 10 Distributions of the absolute total pressure at the outlet of S3 under the design condition

with decreasing *Re*, which was also observed by Diehl et al. (2020). In the tip region, the domain of high loss is not changed, but the loss magnitude is markedly increased because of the effect of a low *Re* on the interactions among the annulus boundary layer, tip leakage flow, and blade boundary layer.

Consequently, the compressor peak efficiency is reduced by a decreasing *Re*. When Re/Re_{ref} is less than 0.2, the decreasing trend in efficiency with *Re* sharpens. Compressor losses increase considerably due to extended boundary layer separations at the blade suction surface, and losses caused by the secondary flow near the hub and shroud increase dramatically at a low *Re*. These two factors cause efficiency degradation at a low *Re*. The empirical approaches proposed by Wassell (1968) and Schaffler (1980) can precisely predict changes in compressor efficiency under the design condition. However, the independent parameters in the correction equations should be adjusted in different ways to predict the efficiency variations under off-design conditions.

4.2 Influence on Stall Mechanisms

As shown in Fig. 4, a decrease in *Re* reduces the stall–pressure ratio. For the sake of clarity, the change in the stall–pressure ratio with decreasing *Re* is shown in Fig. 11. The experimental and numerical results show that the stall–pressure ratio begins to decline sharply when Re/Re_{ref} is lower than 0.2. An empirical approach for predicting the stall–pressure ratio proposed by Wassell (1968) is defined as

$$\frac{\pi_{Ns} - \pi_{Ns,ref}}{\pi_{Ns,ref}} = -0.2\left(\frac{Re}{Re_{ref}}\right)^{n_3} \tag{4}$$

This empirical formula predicted well the change in the stall–pressure ratio with decreasing *Re* for twenty axial compressors. The parameter n_3 is calculated as -0.76 for the three-stage compressor to minimize the fitting standard deviation. The correction equation can precisely predict the critical *Re*, which is 220,000 for the compressor studied. A sharp decrease in the stall–pressure ratio below the critical *Re* implies dramatic changes in the flow fields, which may alter the stall mechanisms.

The stall mechanisms of the compressor under different inlet Reynolds numbers are examined and

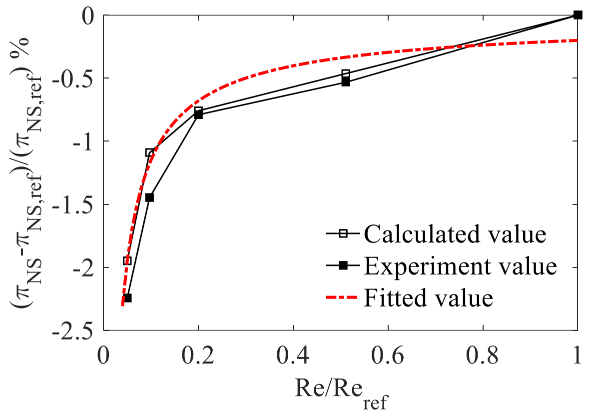

Fig. 11 Normalized changes in the stall–pressure ratio with *Re*

discussed in detail. The "three-step method" proposed in Wang et al. (2020) is adopted to study the effects of *Re* on compressor stall mechanisms. The first and second steps can be performed using only the results of steady simulations, which greatly reduces the amount of calculation effort.

The first step is to observe the pressure rise lines in the compressor maps. The compressor stalls before the compressor characteristics peak at all Reynolds numbers, which indicates that spike-stall inception through short-wavelength disturbances is likely to occur (Camp & Day, 1998).

Determining the stall-limiting location is a challenge in understanding stall mechanisms in a multistage environment. To determine the possible stall-limiting location, the second step involves using a two-dimensional method from the perspective of relative change. The method assumes that the flow under peak-efficiency condition is ideal and that the location where the flow deviates maximally from the ideal flow may trigger stall. Therefore, the relative changes in the relevant aerodynamic parameters between the near-stall condition and the peak-efficiency condition need to be calculated.

The mass flow, which is defined as the product of flow density and the axial component of absolute velocity, is azimuthally averaged in the meridional plane. The relative changes in mass flow between the near-stall condition and the peak-efficiency condition are calculated for the five Reynolds numbers and illustrated in Fig. 12. The negative values represent the decrease in mass flow resulting from throttling of the compressor. The domains of the blades are marked with dashed lines. For the compressor operating at Re/Re_{ref} =1, the mass flow decreases greatly near the tips of R1 and S1, and the downwards trend is stopped at R2. A relatively larger area with decreased mass flow, which is initiated from the hub of S1 (labelled with an ellipse), can be found at lower spans. The domain of the decreased mass flow expands in the radial direction during the process of spreading downstream, and it finally reaches the passage outlet, which occupies nearly 50% of the span. Therefore, the region near the hub of S1, where the flow starts to deviate considerably from the ideal flow, is probably the stall-triggering location. A similar flow situation can be detected under the inlet conditions of Re/Re_{ref} =0.5 and Re/Re_{ref} =0.2.

The distribution of the delta mass flow begins to change when Re/Re_{ref} reaches 0.1, and it is completely different for Re/Re_{ref}=0.05 compared with that of Re/Re_{ref} =1. The area of decreased mass flow from the peak-efficiency condition to the near-stall condition near the hub diminishes at Re/Re_{ref} =0.1 and disappears completely at Re/Re_{ref} =0.05. However, the domain of decreased mass flow near the shroud (labelled with an ellipse) enlarges and ultimately reaches the passage outlet, which occupies nearly 20% of the span. Therefore, the region near the tip of rotor1 can probably trigger stall under the inlet condition of Re/Re_{ref}=0.05.

In the last step of the "three-step method" for understanding stall mechanisms, the flow fields in the possible stall-triggering region will be examined in detail using the results of unsteady simulations. Considering that the flow deterioration regions in the meridian plane are near the hub and the shroud, the instantaneous velocity fields along the 98% span and 5% span are illustrated in Fig. 13 and Fig. 14 for Re/Re_{ref} = 1 and Re/Re_{ref}=0.05 under near-stall conditions at t = 0 *Ts*. *Ts* is equal to the blade passing period of R1. The limiting streamlines on the suction surface of all the blades are presented in Fig. 15 to help understand the flow mechanisms.

For Re/Re_{ref} = 1, the boundary layer is separated at the rear part of the suction surface of R1. In the blade passage of S1, the flow starts to separate from the suction surface at the leading edge, and corner separation occurs near the tip of S1 according to the limiting streamlines. Smaller corner separations can be found at the tips of S2 and S3. However, the flow separation near the shroud is insignificant and does not remarkably reduce the mass flow near the tip region, as shown in Fig. 12 (a). This observation implies that the blade tip will not induce stall. When the compressor operates at Re/Re_{ref} = 0.05, the flow separation near the suction surface nearly blocks the whole blade passage at the tips of R1 and R2. Accordingly, the separation lines shown in Fig. 15 are pushed forward on the blade surfaces, especially at the blade tip region. This severe flow separation causes a decrease in mass flow, and this effect spreads to the aft stage, as shown in Fig. 12 (e), which ultimately triggers the stall of the compressor.

The flow characteristics along the 5% span are completely different from those at the 98% span for the two Reynolds numbers. The flow is severely separated at the suction surfaces of S1, R2, S2, R3, and S3 at Re/Re_{ref} =1, and the corresponding large corner separations can be found by observing the limiting streamlines on the blade surface. The corner separation reduces the mass flow near the hub, and the influence is amplified when the flow travels from S1 to S3, as shown in Fig. 12 (a). This will probably trigger stall of the compressor. For Re/Re_{ref} =0.05, the flow separation region is greatly reduced near the suction surface of S1 and R2 compared with that at Re/Re_{ref} =1. Therefore, the mass flow near the hub does not decrease, as observed in Fig. 12 (e). The observed

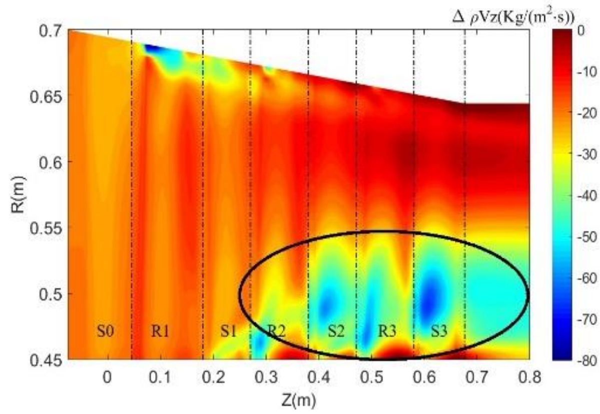

(a) Re/Re_{ref}=1

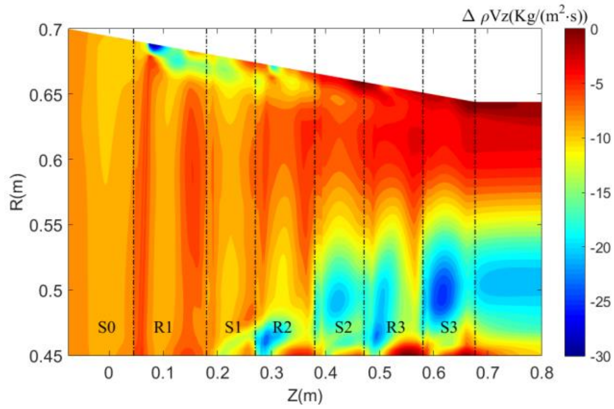

(b) Re/Re_{ref}=0.5

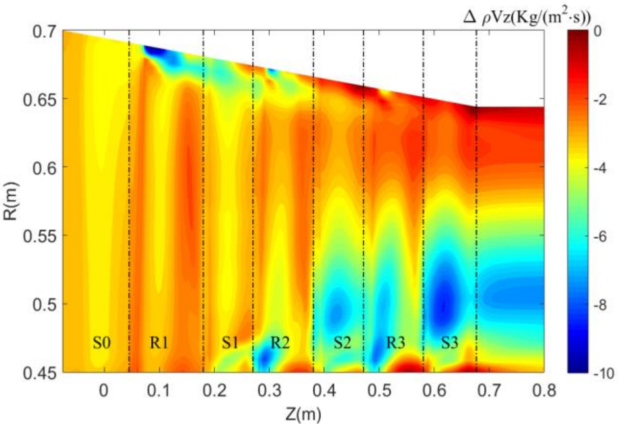

(c) Re/Re_{ref}=0.2

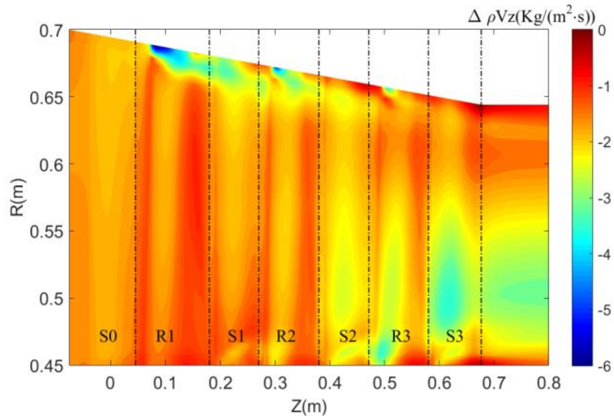

(d) Re/Re_{ref}=0.1

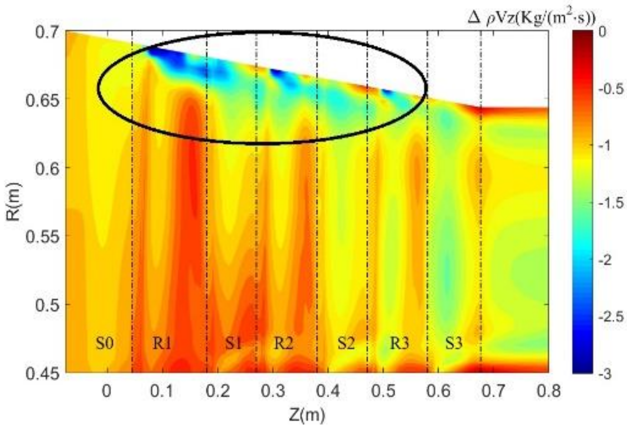

(e) Re/Re_{ref} =0.05

Fig. 12 Relative changes in mass flow between the near-stall condition and peak-efficiency condition

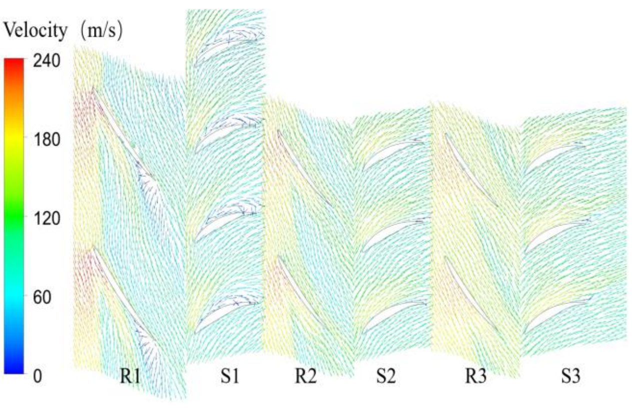

(a) Re/Re_{ref} =1

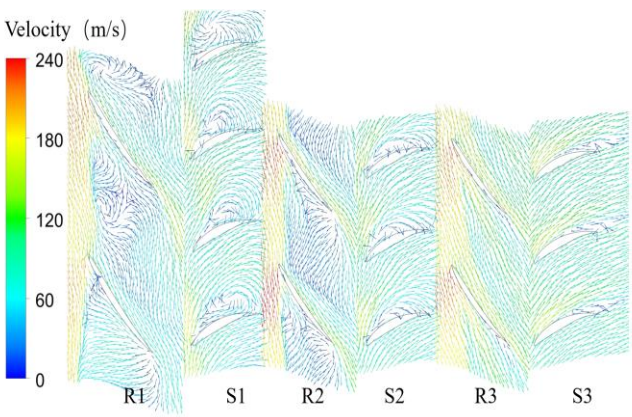

(b) Re/Re_{ref}= 0.05

Fig. 13 Instantaneous distributions of velocity along the 98% span under the near-stall condition at t= 0 *Ts*

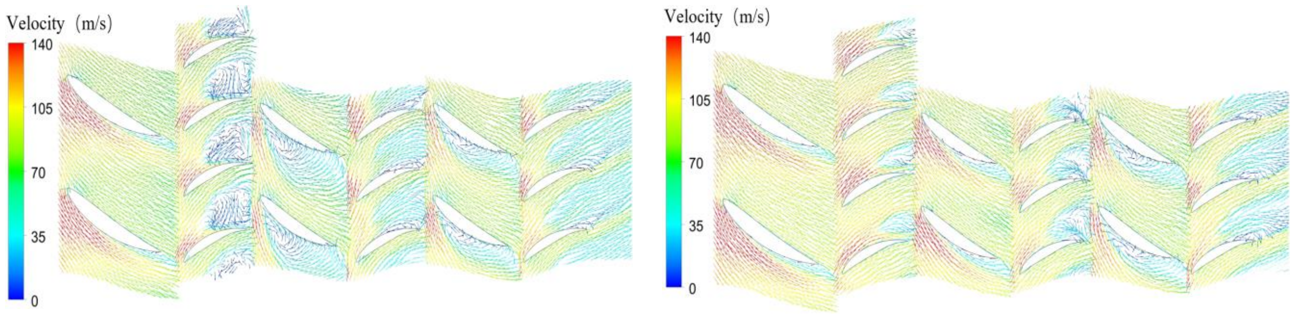

(a) $Re/Re_{\mathrm{ref}}=1$ (b) $Re/Re_{\mathrm{ref}}=0.05$

Fig. 14 Instantaneous distributions of velocity along the 5% span under the near-stall condition at t= 0 *Ts*

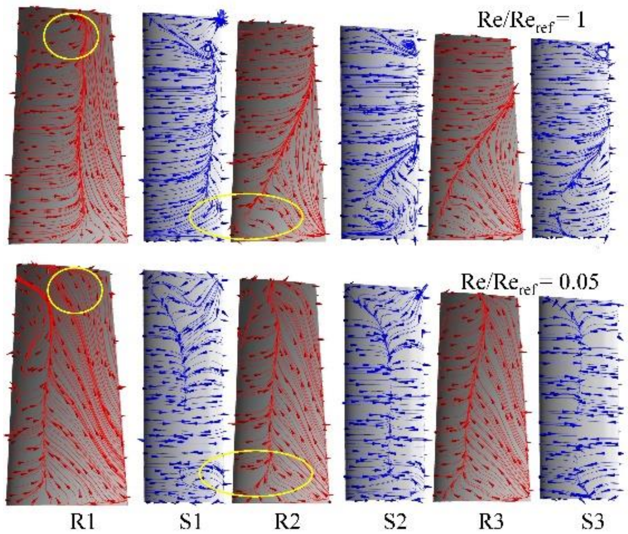

Fig. 15 Instantaneous distributions of limiting streamlines on the blade suction surface under the near-stall condition at t= 0 *Ts*

flow phenomena in the velocity fields are consistent with those proven in the second step, and these observations confirm that the bottom of S1 and the tip of R1 are stall-initiated regions for $Re/Re_{\mathrm{ref}}=1$ and $Re/Re_{\mathrm{ref}}=0.05$, respectively.

The flow in the blade passages of R1 and S1 are examined to understand the reasons for the flow separation introduced above. Figure 16 shows the distributions of the reversed flow regions along the 98% span and the tip leakage flow coloured with the relative velocity in R1 under the near-stall condition. The flow fields at different times, including t=0, 1.5 and 3 *Ts,* are illustrated to understand the unsteady characteristics. When the compressor operates at $Re/Re_{\mathrm{ref}}=0.05$, the tip leakage vortex expands as it processes downstream and interacts with the boundary layer separation, forming a large stagnation zone in blade passage R1_I at t=0 *Ts*; moreover, two small stagnation zones can be observed in blade passage R1_II. As the rotor blade rotates to t=1.5 *Ts*, the sizes of the stagnation zones in different passages

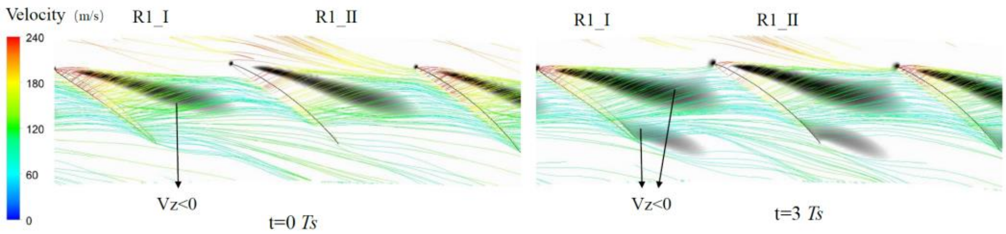

(a) $Re/Re_{\mathrm{ref}}=1$

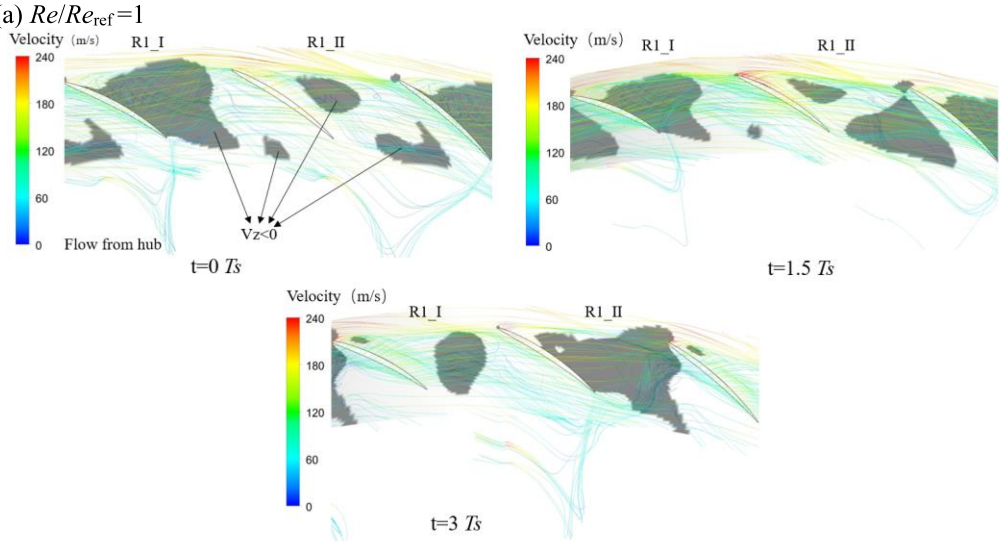

(b) $Re/Re_{\mathrm{ref}}=0.05$

Fig. 16 Instantaneous distributions of the tip leakage flow and regions of reversed flow along the 98% span in R1 under the near-stall condition

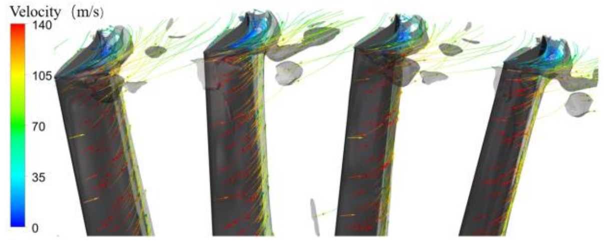

(a) Re/Re_{ref}=1

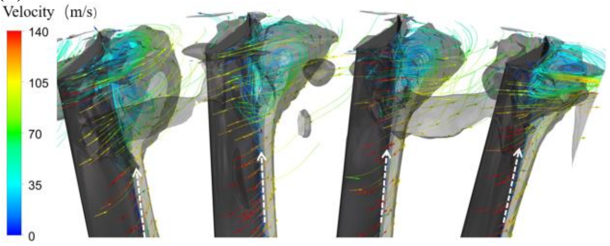

(b) Re/Re_{ref}=0.05

Fig. 17 Instantaneous distributions of separated flow and regions of vortex core near the shroud in S1 under the near-stall condition at t= 0 *Ts*

become nearly the same. The flow distributions in R1_II at t = 3 Ts are almost the same as those in R1_I at t=0 *Ts*. Therefore, the large blockage in the blade passages propagates in the circumferential direction at a relatively lower velocity than the shaft speed, which will probably form a stall cell when throating the compressor deeper. Another observation is that the flow from the hub is transported to the shroud near the blade trailing edge. The stagnation zone in the blade passage becomes more severe when radial transportation occurs. When the compressor operates at Re/Re_{ref}=1, the radial transportation disappears. The passage blockage and flow unsteadiness are very limited.

Figure 17 demonstrates the instantaneous distributions of the vortex evaluated by the λ_2 criterion at the tip of S1 and the streamlines through the vortex core. The vortex is caused by the flow separation near the blade suction surface, which occupies approximately 10% of the span in the radial direction for Re/Re_{ref} = 1. The influence of the vortex disappears in the aft stage, as shown in Fig. 12 (a). When the compressor operates at Re/Re_{ref} = 0.05, the decrease in *Re* enlarges the vortex in the radial and circumferential directions. One reason is the flow deterioration in the blade passage of R1, which increases the attack angle of S1. The other reason is the low-velocity flow being transported from the hub along the blade surface (dashed arrow), which exacerbates the flow separation at the blade suction surface. The vortex occupies nearly 25% of the span in the radial direction and more than half the blade passage in the circumferential direction. The effect of the vortex does not disappear in the aft stage, but it causes flow separation at the suction surface of all the blades. Moreover, unsteady changes in the blockage similar to those for R1 in Fig. 16 are not detected in the stator by observing the flow fields at different times (not shown).

Figure 18 shows the instantaneous distributions of the vortex evaluated by the λ_2 criterion at the hub of S1 and the streamlines of leakage flow through the gap between the stator blade and the hub. The vortex is

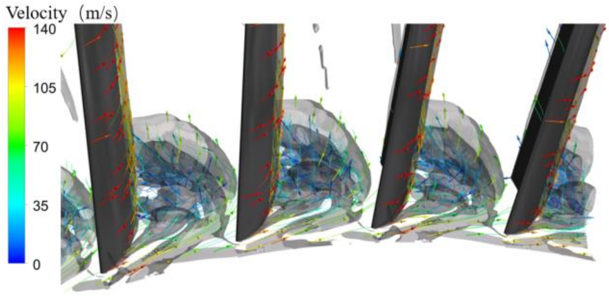

(a) Re/Re_{ref} =1

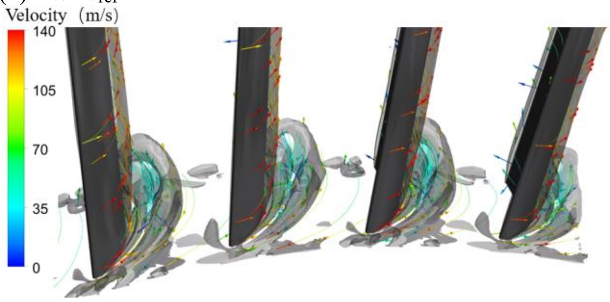

(b) Re/Re_{ref}=0.05

Fig. 18 Instantaneous distributions of separated flow and regions of vortex core near the hub in S1 under the near-stall condition at t= 0 *Ts*

induced by the interactions between the flow separation near the blade suction surface and the leakage flow, which occupies approximately 15% of the span in the radial direction and nearly fills the whole blade passage in the circumferential direction at Re/Re_{ref}=1. As Re/Re_{ref} is reduced to 0.05, the domain of the vortex is greatly reduced, and the effect of the vortex disappears in the aft stage, as shown in Fig. 12 (e).

Consequently, the hub of S1 is the probable stall-initiated location when the compressor operates at high *Re*, and the tip of R1 may induce stall when *Re* is very low. The interaction between the boundary layer separation and the leakage flow through the gaps between the blade and the end wall causes a large vortex, which blocks the blade passage. The blocking effect spreads to the aft stage along the hub at Re/Re_{ref}=1 and along the shroud at Re/Re_{ref}=0.05, which triggers the stall of the whole compressor.

The discussion above mainly concerns the factors that can induce stall at different Reynolds numbers. The formation and propagation of stall cells in spike-type stalls are not discussed because of limited computational resources for implementing full-annulus unsteady simulations. The mechanism of spike-type stall, which is induced by a tip leakage vortex, has been discussed extensively (Tan et al., 2010) and can help us understand the stall mechanism of the three-stage compressor at Re/Re_{ref}=0.05. However, the characteristics of stall induced by the vortex near the hub in the stator (Re/Re_{ref} =1) in a multistage environment are poorly understood and should receive increased attention in future studies.

4.3 Mechanism of the *Re* Effect on the Flow Characteristics

To understand the reasons for the flow variations caused by changing the Reynolds number, Fig. 19 shows

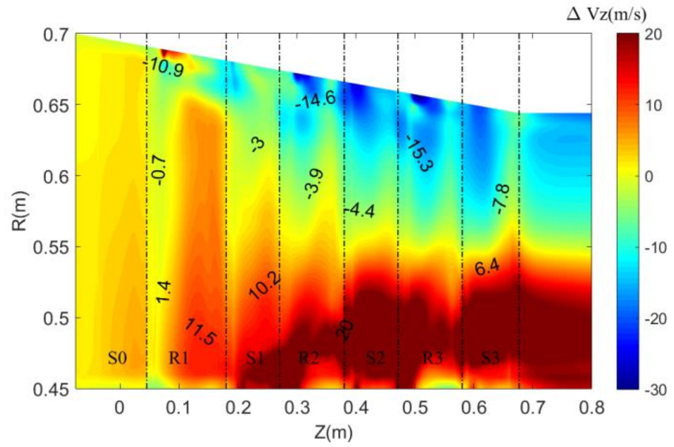

(a) Axial component of the velocity

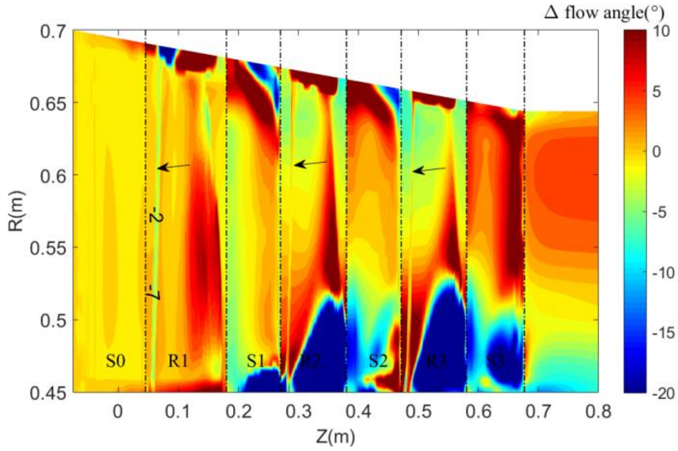

(b) Flow angle

Fig. 19 Relative changes in flow parameters between Re/Re_{ref} =1 and Re/Re_{ref} =0.05 in the meridional plane under the near-stall condition

a comparison of the azimuthally averaged axial component of the velocity and flow angle (angle between the velocity and the axial direction) in the meridional plane for Re/Re_{ref} =1 and Re/Re_{ref} = 0.05 under the near-stall condition. A negative value represents a reduction caused by a decrease in *Re*. The axial velocity at the inlet is nearly unchanged along the whole span, but it begins to change when the flow travels into R1. The axial velocity increases below the 80% span and decreases at the upper 20% span. The flow redistribution is amplified in the aft stage, especially in the regions near the shroud and the hub due to flow separation (Fig. 17 and Fig. 18). The flow angle near the blade leading edge (labelled with arrow) is reduced for all the rotor blades, especially in R1. However, the flow angle is improved at the rear part of the rotor blades because the separation lines are pushed forward, as shown in Fig. 15. The significant changes in the flow angle near the shroud and the hub are caused by the change in the flow separation (Fig. 17 and Fig. 18). Therefore, the flow is redistributed along the span, and the aerodynamics of the blades change with decreasing *Re*.

Figure 20 shows the pressure coefficient (*Cp*) along the chord of R1 along 98%, 50% and 5% spans under the near-stall condition. The difference in *Cp* between the pressure and suction sides, which represents the blade loading, is also calculated. The pressure distribution is remarkably changed near the leading edge by changing *Re*, especially at the 98% span. The blade loading is reduced upstream by approximately 50%, 40%, and 30% of the axial chord length at 98%, 50%, and 5% spans, respectively. The extent of the depressed blade loading increases with increasing blade height. At the rear part of the blade, the blade loading is unchanged at the 98% span and improved at the 50% and 5% spans. This result is consistent with the changes in the flow angle shown in Fig. 19 (b).

The inlet Reynolds numbers at different blade heights differ, which changes the aerodynamic performance of each blade element at different spans to varying degrees. As a result, the radial balance in the blade passage changes, which results in radial transportation, as shown in Fig. 16 and Fig. 17. The radial transportation significantly influences the extent of the vortex caused by the interaction between the boundary-layer separation and the leakage flow. This phenomenon ultimately changes the stall-triggering location under different inlet Reynolds numbers. Therefore, the blade profile can be redesigned to make the radial balance constant under different Reynolds numbers for keeping the stall-initiated region unchanged to enhance the stability of the compressor conveniently. The other option is to adjust the angles of IGV and stators to change the radial balance, which will be studied in the future.

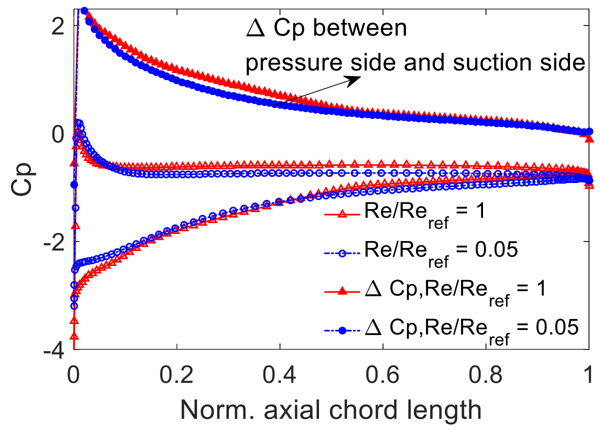

(a) 98% span

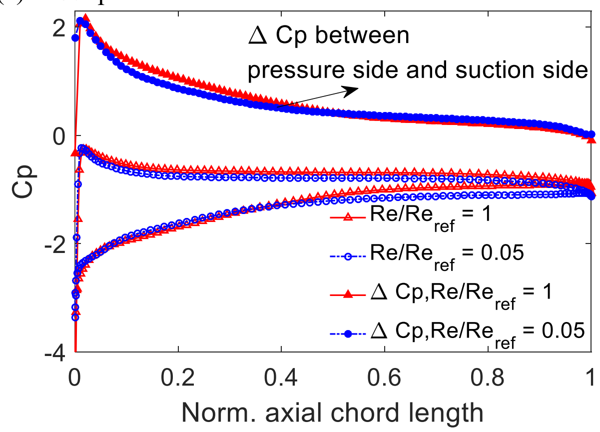

(b) 50% span

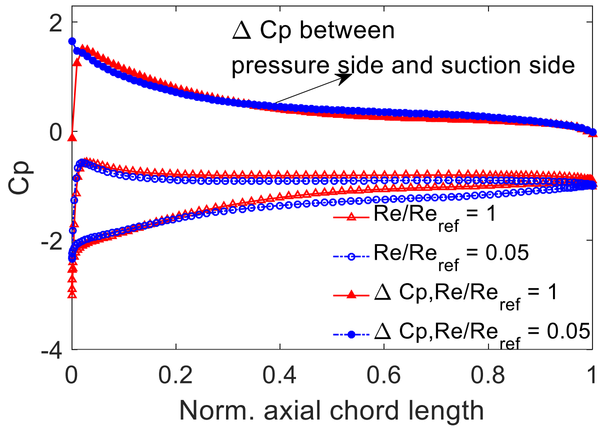

(c) 5% span

Fig. 20 Distributions of Cp along the blade chord at two Reynolds numbers

5. CONCLUSIONS

The main conclusions can be summarized as follows:

1. The experimental and numerical results show that the Re significantly influences compressor performance below a critical value of 220,000. The compressor efficiency is reduced by 9%, and the stall–pressure ratio is decreased by 1.95% when *Re* is changed from 1,100,000 to 55,000. Empirical approaches can predict the efficiency variations due to the decrease in *Re* under the design condition. However, the independent parameters should be altered to calculate the compressor efficiency under off-design conditions.

2. For the design condition, the decrease in *Re* increases the loss in the blade wake of the rotors and stators because of the extended boundary layer separations at the blade suction surface. Such a decrease also increases losses near the hub and shroud, which are caused by secondary flow. The latter plays an important role in efficiency degradation at a low *Re*.

3. The stall mechanisms are different at various inlet Reynolds numbers. The hub of stator 1, where the interaction between the corner separation and leakage flow through the stator blade hub gap causes a large vortex and passage blockage, induces stall at higher Reynolds numbers. However, the tip of rotor 1 triggers stall because of the interaction between the blade boundary layer separation and tip leakage flow at low *Re*.

4. The rotor blade loading distributions change with decreasing *Re* for the stall-initiated stage, and this effect varies for blade elements at different spans. As a result, the radial balance in the blade passage changes, which alters the radial flow transportation and then the vortex extent near the end wall. This phenomenon ultimately changes the stall mechanisms of the compressor at different Reynolds numbers. Therefore, both the shroud and hub should be considered when installing facilities such as casing treatment to enhance the stability of the compressor for a wide range of Reynolds numbers.

CONFLICT OF INTERESTS

The authors have no competing interests and conflicts to disclose.

AUTHORS CONTRIBUTION

E. Zhou: Conceptualization, Project administration, Review and Editing; **P. Lei**: Data curation, Formal analysis, Software, Writing original draft; **C. Fan**: Resources; **W. Zhang**: Validation; **K. Liu**: Validation; and **S. Cheng**: Supervision.

REFERENCES

Arshad, A., Li, Q., Li, S., & Pan, T. (2018). Effects of inlet radial distortion on the type of stall precursor in low-speed axial compressor. *Proceedings of the Institution of Mechanical Engineers Part G-Journal of Aerospace Engineering*, *232*(1), 55-67. https://doi.org/10.1177/0954410016670679

Back, S. C., Hobson, G. V., Song, S. J., & Millsaps, K. T. (2010). Effect of surface roughness location and Reynolds number on compressor cascade performance. *ASEM Paper*, GT2010-22208. https://doi.org/10.1115/GT2010-22208

Back, S. C., Hobson, G. V., Song, S. J., & Millsaps, K. T. (2012). Effects of Reynolds number and surface roughness magnitude and location on compressor cascade performance. *Journal of Turbomachinery*, *134*(5), 051013-1~051013-6. https://doi.org/10.1115/1.4003821

Bolinches-Gisbert, M., Robles, D. C., Corral, R., &

Gisbert, F. (2020). Prediction of Reynolds number effects on low-pressure turbines using a high-order ILES method. *Journal of Turbomachinery, 142* (3), 031002. https://doi.org/10.1115/1.4045776

Camp, T. R., & Day, I. J. (1998). A study of spike and modal stall phenomena in a low-speed axial compressor. *ASME Journal of Turbomachinery*, *120*, 393-401. https://doi.org/10.1115/97-GT-526

Carullo, J. S., Nasir, S., Cress, R. D., Ng, W. F., & Thole, K. A. (2011). The effects of freestream turbulence, turbulence length scale, and exit Reynolds number on turbine blade heat transfer in a transonic cascade. *Journal of Turbomachinery*, *133*(1), 011030. https://doi.org/10.1115/1.4001366

Chen, H. (2020). Size and Reynolds number effects on compressor performance and scaling. *ASME Paper*, GT2020-14019. https://doi.org/10.1115/GT2020-14019

Chen, Z. Y., Wu, Y. H., Zhang, Y. W., Gan, J. W., & Jin, H. Y. (2019). Circumferential propagation characteristic of unsteady flow in a subsonic axial flow compressor rotor at different Reynolds numbers. *ASME Paper*, GT2019-91498. https://doi.org/ 10.1115/GT2019-91498

Citavy, J., & Norbury, J. F. (1977). Effect of Reynolds number and turbulence intensity on the performance of a compressor cascade with prescribed velocity distribution. *Journal of Mechanical Engineering Science*, *19*(3), 93-100. https://doi.org/10.1243/JMES_JOUR_1977_019_022_02

Diehl, M., Schreiber, C., & Schiffmann, J. (2020). The role of Reynolds number effect and tip leakage in compressor geometry scaling at low turbulent Reynolds numbers. *Journal of Turbomachinery*, *142*(3), 031003. https://doi.org/ 10.1115/1.4045465

Enomoto, S., Hah, C., & Hobson, G. V. (2000). Numerical and experimental investigation of low Reynolds number effects on laminar flow separation and transition in a cascade of compressor blades. *ASME Paper*, GT2000-0276.

Farahani, A. S., Amiri, H. B., Khazaei, H., Madadi, A., & Fathi, A. (2012). The Effect of Reynolds number on transonic compressor blade rotor section. *ASME Paper*, GTINDIA2012-9639. https://doi.org/10.1115/GTINDIA2012-9639

Hadavandi, R., Fontaneto, F., & Desset, J. (2018). Complete characterization of a highly loaded low pressure compressor at different Reynolds numbers for computational fluid dynamics simulations. *Journal of Turbomachinery*, *140*(6), 061008. https://doi.org/ 10.1115/1.4039727

Hathaway, M. D. (2007). Passive endwall treatments for enhancing stability. *NASA Report*, NASA/TM-2007-214409.

Hayashibara, S., Myose, R. Y., & Kok, F. (2013). *Effect of solidity on the generation of entropy in a low Reynolds number compressor cascade.* 2013 Aviation Technology, Integration, and Operations Conference, AIAA 2013-4416.

Hayashibara, S., Myose, R. Y., Mark, R. D., & Walsh, E. D. (2006). *Determining the entropy generated in a low Reynolds number compressor cascade based on the wake velocity profile.* 6th AIAA Aviation Technology, Integration, and Operations Conference, AIAA 2006-7810.

Hobson, G. V., Hansen, D. J., Schnorenberg, D. G., & Grove, D. V. (2001). Effect of Reynolds number on separation bubbles on compressor blades in cascade. *Journal of Propulsion and Power*, *17*(1), 154-162. https://doi.org/10.2514/2.5721

Hutchings, J., & Hall, C. (2020). The effects of Reynolds number on the stall and pre-stall behaviour of compact axial compressors. *ASME Paper*, GT2020-15384. https://doi.org/ 10.1115/GT2020-15384

Im, J. H., Shin, J. H., Hobson, G. V., Song, S. J., & Millsaps, K. T. (2013). Effect of leading edge roughness and Reynolds number on compressor profile loss. *ASME Paper*, GT2013-95487. https://doi.org/ 10.1115/GT2013-95487

Kato, H., Taniguchi, H., Matsuda, K., Funazaki, K., Kato, D., & Pallot, G. (2011). Experimental and numerical investigation on compressor cascade flows with tip clearance at a low Reynolds number condition. *Journal of Thermal Science*, *20*(6), 481-485. https://doi.org/10.1007/s11630-011-0499-9

Kim, J., Jeon, H., Jung, Y., Park, J. Y., & Choi, M. (2018). Effects of low Reynolds number on performance in a centrifugal compressor. *Transactions of the Japan Society for Aeronautical and Space Sciences*, *61*(6), 238-247. https://doi.org/10.2322/tjsass.61.238

Kok, F., Myose, R. Y., & Hayashibara, S. (2015). *Comparison of theoretical and semi-empirical solutions for dissipation coefficient in a low Reynolds number compressor cascade.* 45th AIAA Fluid Dynamics Conference, AIAA 2015-2314. https://doi.org/10.2514/6.2015-2314

Lazaro, B. J., Gonzalez, E., Cadrecha, D., Antoranz, A., & Parra, J. (2017). Low Reynolds number response of high efficiency, intermediate pressure compressor profiles. *ASME Paper*, GT2017-63283. https://doi.org/10.1115/GT2017-63283

Maffioli, A., Hall, C. A., & Melvin, S. (2015). Aerodynamics of low Reynolds number axial compressor sections. *53rd AIAA Aerospace Sciences Meeting*, AIAA 2015-1934. https://doi.org/10.2514/6.2015-1934

Matthias, R., Martin, L., Konrad, V., & Ronald, M. (2017). Experimental and numerical investigation of a circumferential groove casing treatment in a low speed axial research compressor at different tip clearances. *ASME Paper*, GT2017-6305. https://doi.org/10.1115/GT201763051

McDougall, N. M., Cumpsty, N. A., & Hynes, T. P. (1990). Stall inception in axial compressors. *Journal of Turbomachinery*, *112*, 116-125. https://doi.org/10.1115/89-GT-63

Myose, R. Y., & Hayashibara, S. (2009). *Effect of stagger angle on the generation of entropy in a low Reynolds number compressor cascade*. 9th AIAA Aviation Technology, Integration and Operations (ATIO) Conference, AIAA 2009-6940. https://doi.org/10.2514/6.2009-6940

Myose, R. Y., Lietsche, J., Scholz, D., Zingel, H., Hayashibara, S., & Heron, I. (2006). *Flow visualization study on the effect of a Gurney flap in a low Reynolds number compressor cascade*. 6th AIAA Aviation Technology, Integration, and Operations Conference, 2: 992-1002. https://doi.org/10.2514/6.2006-7809

Ni, Y., Chen, J., Fu, X., Huang, G., Zhang, Z., & Zhu, R. (2019). Flow characteristics of centrifugal compressor stage under low Reynolds number. *The Proceedings of the 2018 Asia-Pacific International Symposium on Aerospace Technology*, *459*, 513-522. https://doi.org/10.1007/978-981-13-3305-7_42

Pantelidis, K., & Hall, C. A. (2017). *Reynolds number effects on the aerodynamics of compact axial compressors*. 12th European Conference on Turbomachinery Fluid Dynamics and Thermodynamics, ETC2017-277. https://doi.org/10.29008/etc2017-277

Pym, S. A., Asghar, A., Allan, W. D. E., & Clark, J. P. (2019). A low Reynolds number experimental evaluation of tubercles on a low-pressure turbine cascade. *ASME Paper*, GT2019-91699. https://doi.org/10.1115/GT2019-91699

Schaffler, A. (1980). Experimental and analytical investigation of the effects of Reynolds number and blade surface roughness on multistage axial flow compressors. *Journal of Engineering for Power*, *102*, 5-12. https://doi.org/10.1115/1.3230232

Schreiber, H., Steinert, W., & Kusters, B. (2002). Effects of Reynolds number and free-stream turbulence on boundary layer transition in a compressor cascade. *Journal of Turbomachinery*, *124*(1), 1-9. https://doi.org/10.1115/1.1413471

Schreiber, H., Steinert, W., Sonoda, T., & Arima, T. (2004). Advanced high-turning compressor airfoils for low Reynolds number condition - Part II: Experimental and numerical analysis. *Journal of Turbomachinery*, *126*(4), 482-492. https://doi.org/10.1115/1.1737781

Sonoda, T., Yamaguchi, Y., Arima, T., Olhofer, M., Sendhoff, B., & Schreiber, H. (2003). Advanced high turning compressor airfoils for low Reynolds number condition Part1: Design and optimization. *ASME Paper*, GT2003-38458. https://doi.org/10.1115/GT2003-38458

Sun, D., Li, J., Dong, X., Gu, B., Sun, X. (2018). Effects of rotating inlet distortion on two-stage compressor stability with stall precursor-suppressed casing treatment. *ASME Paper*, GT2018-76701. https://doi.org/10.1115/GT2018-76701

Tan, C. S., Day, I., Morris, S., & Wadia, A. (2010). Spike-type compressor stall inception, detection, and control. *Annual Review of Fluid Mechanics*, *42*, 275-300. https://doi.org/10.1146/annurev-fluid-121108-145603

Toyotaka, S., Yoshihiro, Y., Toshiyuki, A., Markus, O., Bernhard, S., & Heinz A. S. (2003). Advanced high turning compressor airfoils for low Reynolds number condition part1: design and optimization. *ASME paper*, GT2003-38458. https://doi.org/10.1115/GT2003-38458

Valdes, M., Sebastian, A., & Abbas, R. (2018). Reynolds-number-dependent efficiency characterization of a micro-scale centrifugal compressor using non-conventional working fluids. *Energy Conversion and Management*, 177, 224-232. https://doi.org/10.1016/j.enconman.2018.09.055

Wang, M., Li, Z., Zhao, S., Zhang, Y., & Lu, X. (2020). Effects of Reynolds number and loading distribution on the aerodynamic performance of a high subsonic compressor airfoil. *Proceedings of the Institution of Mechanical Engineers, Part A: Journal of Power and Energy*, *234*(8), 1069-1083. https://doi.org/10.1177/0957650919899541

Wang, M., Yang, C., Li, Z., Zhao, S., Zhang, Y., & Lu, X. (2021). Effects of surface roughness on the aerodynamic performance of a high subsonic compressor airfoil at low Reynolds number. *Chinese Journal of Aeronautics*, *34* (3), 71-81. https://doi.org/10.1016/j.cja.2020.08.020

Wang, W., Lu, J., Luo, X., Huang, R., & Chu, W. (2020). Failure mechanism of slot casing treatment in improving stability of a highly-loaded axial compressor stage. *Aerospace Science and Technology*, *105*, 105979. https://doi.org/10.1016/j.ast.2020.105979

Wassell, A. B. (1968). Reynolds number effects in axial compressors. *Journal of Engineering for Power*, *149*, 156. https://doi.org/10.1115/1.3609154

Weinberg, M., & Wyzykowski, J. (2001). Development and testing of a commercial turbofan engine for high altitude UAV applications. SAE Technical Papers, 2001, SAE World Aviation Congress - 2001 Aerospace Congress. https://doi.org/10.4271/2001-01-2972

Wilke, I., Kau, H. P., & Brignole, G. (2005). Numerically aided design of a high-efficient casing treatment for a transonic compressor. *ASME Paper*, GT2005-68993. https://doi.org/10.1115/GT2005-68993

Zhang, W., Zhou, E., Cheng, S., & Liu, K. (2017). Anti-surge model and control strategy of fan in wind tunnel. *Journal of Aerospace Power*, 32(6), 1434-1440(Chinese). https://doi.org/10.13224/j.cnki.jasp.2017.06.021

Zhang, X. (2020). Effects of Reynolds number on performance of highly loaded multi-stage axial compressors. *ASME Paper*, GT2020-14672. https://doi.org/10.1115/GT2020-14672

Zhao, S., Lu, X., Zhu, J., Ge, H., & Yang, C. (2015). Effects of low Reynolds number on flow stability of a transonic compressor. *Proceedings of the Institution of Mechanical Engineers Part G-Journal of Aerospace Engineering*, *229*(4), 601-611. https://doi.org/10.1177/0954410014537803

Zheng, X., Lin, Y., Gan, B., Zhuge, W., & Zhang, Y. (2013). Effects of Reynolds number on the performance of a high pressure-ratio turbocharger compressor. *Science China-Technological Sciences*, 56(6), 1361-1369. https://doi.org/10.1007/s11431-013-5213-6

Zhou, E., Cheng, S., Liu, K., Zhang, W., & Wang, Y. (2015). Study of the compressor system's debugging in 0.6m continuous wind tunnel. *Fluid Machinery*, 43(11), 10-15(Chinese). https://doi.org/10.3969/j.issn.1005-0329.2015.11.003